Original Article

Malignant pleural mesothelioma nodules remodel their surroundings to vascularize and grow

Ildiko Kovacs[1], Edina Bugyik[1], Katalin Dezso[2], Julia Tarnoki-Zach[3], Elod Mehes[1,3], Marton Gulyas[3], Andras Czirok[3,4], Elisabeth Lang[5], Michael Grusch[5], Karin Schelch[5,6], Balazs Hegedus[7], Ildiko Horvath[1], Nandor Barany[1,6], Zsolt Megyesfalvi[1,6,8], Anna Tisza[1,2], Zoltan Lohinai[1], Mir Alireza Hoda[6], Konrad Hoetzenecker[6], Francesco Pezzella[9], Sandor Paku[2], Viktoria Laszlo[1,6]*, Balazs Dome[1,6,8]*

[1]National Koranyi Institute of Pulmonology, Budapest, Hungary; [2]1st Department of Pathology and Experimental Cancer Research, Semmelweis University, Budapest, Hungary; [3]Department of Biological Physics, Eotvos University, Budapest, Hungary; [4]Department of Anatomy & Cell Biology, University of Kansas Medical Center, Kansas City, KS, USA; [5]Institute of Cancer Research, Department of Medicine I, Medical University of Vienna, Vienna, Austria; [6]Department of Thoracic Surgery, Medical University of Vienna, Vienna, Austria; [7]Department of Thoracic Surgery, Ruhrlandklinik, University Clinic Essen, Essen, Germany; [8]Department of Thoracic Surgery, National Institute of Oncology-Semmelweis University, Budapest, Hungary; [9]Nuffield Division of Laboratory Science, Radcliffe Department of Medicine, University of Oxford, John Radcliffe Hospital, Oxford, UK

Contributions: (I) Conception and design: V Laszlo, B Dome; (II) Administrative support: B Dome, B Hegedus, E Lang, M Grusch, V Laszlo; (III) Provision of study materials or patients: I Kovacs, E Bugyik, F Pezzella, S Paku, V Laszlo, B Dome, Z Megyesfalvi, N Barany, K Dezso, J Tarnoki-Zach, E Mehes, M Grusch, A Czirok, A Tisza, Z Lohinai, I Horvath, K Hoetzenecker; MA Hoda; (IV) Collection and assembly of data: I Kovacs, E Bugyik, F Pezzella, S Paku, V Laszlo, B Dome, Z Megyesfalvi, N Barany, K Dezso, J Tarnoki-Zach, E Mehes, M Grusch, A Czirok, A Tisza, Z Lohinai, I Horvath, K Hoetzenecker; (V) Data analysis and interpretation: I Kovacs, A Tisza, Z Megyesfalvi, Z Lohinai, E Lang, M Grusch, K Schelch, B Hegedus, V Laszlo; (VI) Manuscript writing: All authors; (VII) Final approval of manuscript: All authors.

*These authors share the last authorship.

Correspondence to: Balazs Dome, MD, PhD; Viktoria Laszlo, MSc, PhD. Department of Thoracic Surgery, Medical University of Vienna, Waehringer Guertel 18-20, A-1090 Vienna, Austria. Email: balazs.dome@meduniwien.ac.at; viktoria.laszlo@meduniwien.ac.at.

Background: The microanatomical steps of malignant pleural mesothelioma (MPM) vascularization and the resistance mechanisms to anti-angiogenic drugs in MPM are unclear.

Methods: We investigated the vascularization of intrapleurally implanted human P31 and SPC111 MPM cells. We also assessed MPM cell's motility, invasion and interaction with endothelial cells *in vitro*.

Results: P31 cells exhibited significantly higher two-dimensional (2D) motility and three-dimensional (3D) invasion than SPC111 cells *in vitro*. In co-cultures of MPM and endothelial cells, P31 spheroids permitted endothelial sprouting (ES) with minimal spatial distortion, whereas SPC111 spheroids repealed endothelial sprouts. Both MPM lines induced the early onset of submesothelial microvascular plexuses covering large pleural areas including regions distant from tumor colonies. The development of these microvascular networks occurred due to both intussusceptive angiogenesis (IA) and ES and was accelerated by vascular endothelial growth factor A (VEGF-A)-overexpression. Notably, SPC111 colonies showed different behavior to P31 cells. P31 nodules incorporated tumor-induced capillary plexuses from the earliest stages of tumor formation. P31 cells deposited a collagenous matrix of human origin which provided "space" for further intratumoral angiogenesis. In contrast, SPC111 colonies pushed the capillary plexuses away and thus remained avascular for weeks. The key event in SPC111 vascularization was the development of a desmoplastic matrix of mouse origin. Continuously invaded by SPC111 cells, this matrix transformed into intratumoral connective tissue trunks, providing a route for ES from the diaphragm.

Conclusions: Here, we report two distinct growth patterns of orthotopically implanted human MPM xenografts. In the invasive pattern, MPM cells invade and thus co-opt peritumoral capillary plexuses. In the pushing/desmoplastic pattern, MPM cells induce a desmoplastic response within the underlying tissue which allows the ingrowth of a nutritive vasculature from the pleura.

Keywords: Mesothelioma; vascularization; angiogenesis; orthotopic mouse model of mesothelioma

Submitted Oct 12, 2021. Accepted for publication Apr 24, 2022.
doi: 10.21037/tlcr-21-828
View this article at: https://dx.doi.org/10.21037/tlcr-21-828

Introduction

Malignant pleural mesothelioma (MPM) is an extremely aggressive asbestos-related neoplasm originating from the pleural mesothelium (1,2). It is usually diagnosed at an advanced stage, and is characterized by poor prognosis and resistance to conventional chemotherapies (3). Surgery may be appropriate only at the early stage of the disease. The majority of patients with non-resectable MPM receives systemic treatment. The combination of cisplatin and pemetrexed is the first-line standard chemotherapy for MPM patients since 2009 (4).

Therapeutic approaches for MPM have not yet benefited considerably from the paradigm shift of personalized medicine. Previous studies showed that certain pro-angiogenic cytokines, including vascular endothelial growth factors (VEGFs), are overexpressed both in the tissue and serum samples of MPM patients (5-7). Accordingly, in preclinical studies, anti-angiogenic therapies showed promising results (8-10). Furthermore, in 2016, the MAPS trial reported survival benefit of the addition of bevacizumab, an anti-VEGF antibody, to cisplatin/pemetrexed. This combination has become standard of care in a few countries, but not worldwide (11). Of note, our group reported that nintedanib also has significant antitumor activity in preclinical MPM models (12). In line with this, the addition of nintedanib to the cisplatin-pemetrexed regimen resulted in improved progression-free survival (PFS) in the phase II LUME-MESO clinical trial. However, the subsequent phase III study failed to confirm this benefit (13,14). Notably, several other anti-vascular molecules were tested against MPM with no real advantage yet (15-20). Overall, unfortunately there has not been a real breakthrough in the treatment of MPM with anti-vascular or with other targeted agents (21). Nevertheless, in well-selected patient subpopulations, combination with bevacizumab might result in a significant improvement of survival outcomes (11,22). Therefore, in order to implement personalized therapeutic approaches concerning antiangiogenic agents in mesothelioma patients, identifying novel biomarkers of response are crucial, as well as evaluating the mechanisms of vascularization of MPM (22).

Our knowledge about the microanatomy of vascularization in MPM is limited. In general, tumors gain their vasculature through various mechanisms. The most common forms are capillary sprouting and IA, both involving endothelial proliferation (23). Besides tumor-derived fibrogenic signals (24), host-tissue microenvironment also has an influence on the vascularization type of developing neoplasms (25). In solid tumors, malignant and stromal cell populations are embedded in extracellular matrix (ECM) that is able to affect cell migration and specific signaling pathways (26). VEGF expression increases the permeability of vessels, that leads to protein extravasation and subsequently to a fibrin-rich stroma supporting the migration of endothelial and perivascular cells (27).

Despite the strong rationale, a truly effective anti-angiogenic strategy has not been developed for MPM therapy, and little is known about the specific vascularization mechanisms which are crucial to explore for the implementation of personalized therapeutic approaches in the future. In the present study, we aimed to gain insights into the motility, invasion and vascularization of intrapleurally implanted human MPM cell lines, and to assess the role of VEGF-A in vascular plexus formation. We present the following article in accordance with the ARRIVE reporting checklist (available at https://tlcr.amegroups.com/article/view/10.21037/tlcr-21-828/rc).

Methods

Cell lines

SPC111 cells were established from human biphasic MPM and kindly provided by Prof. R. Stahel (University of Zurich, Zurich, Switzerland; RRID:CVCL D311). P31 (epithelioid MPM) cells were kindly provided by Prof. K. Grankvist (University of Umea, Umea, Sweden). Both cell lines were maintained in RPMI-1640 (Sigma Aldrich, St. Louis, MO, R8758-500ml) or DMEM (Sigma Aldrich, St. Louis, MO, R5796-500ml) culture media supplemented with 10% Fetal Bovine Serum (FBS, Sigma Aldrich, St. Louis, MO, F9665) and 1% penicillin-streptomycin (Sigma Aldrich, St. Louis, MO, P4458-100ml) solution. HUVEC

primary endothelial cells were purchased from Lonza and maintained in EGM2 medium (Lonza). The cells were cultured in non-precoated culture dishes in a humidified incubator at 37 ℃ with 5% CO_2.

Besides the abovementioned MPM cell lines, we also used VEGF-A overexpressing SPC111 (SPC111-RFP-VEGF-A), SPC111-RFP, SPC111-mCherry and P31-mCherry cells. These transgenic cell lines were generated by infection with replication incompetent pseudotyped retroviruses and subsequent antibiotic selection. For that, the open reading frames of mCherry, RFP or VEGFA121 were subcloned into the retroviral expression plasmids pQCXIP or pQCXIN from Clontech. The retroviral expression plasmids were then co-transfected into HEK293 cells with the helper plasmids pVSV-G and p-gag-pol-gpt to generate viral particles. Viral particles were harvested after 72 hours and used for infection of target cells without enrichment. MPM cells stably expressing the transgenes from the pQCXIP or pQCXIN constructs were selected by treatment with puromycin (0.8 µg/mL) or G-418 (500 µg/mL), respectively, for two weeks. The study was conducted in accordance with the Declaration of Helsinki (as revised in 2013).

Spheroid formation

For endothelial sprout growth assay, HUVEC, P31 and SPC111 spheroid aggregates were created by seeding cells in aggregation chambers that do not support cell adherence. The chambers were then incubated in EGM-2 medium (Lonza) for 1 day allowing cells to self-organize into spheroid aggregates. These aggregates were collected and embedded in 3 mg/mL fibrin gel prepared as described earlier (28). Briefly, 3 mg/mL human fibrinogen was combined with 200 U/mL aprotinin, 2 U/mL human thrombin, 2.5 mM $CaCl_2$ (all from Sigma) and 2 U/mL human factor XIII (CSL Behring), then HUVEC and P31 or SPC111 aggregates were added and the solution was transferred and allowed to gelate in circular wells. These 6 mm diameter circular open wells of 50 µL volume were created by filament-deposition ("3D") printing (Ultimaker V2) of poly-lactic acid (PLA) well walls in 35-mm tissue culture dishes (Greiner) using a customized technique described recently (29). Fibrin gels containing the two types of spheroid aggregates were covered with 3 mL EGM-2 medium supplemented with 40 ng/mL bFGF, 40 ng/mL VEGF (Pierce), 80 nM PMA (Fluka), and 50 µg/mL ascorbic acid (Sigma) as described earlier (30) and they were kept at 37 ℃ in a humidified incubator with 5% CO_2 atmosphere. Spheroid size ranged between 300 and 400 µm of diameter.

Time-lapse videomicroscopy

Time-lapse recordings of endothelial sprout growth assays were performed on a Zeiss Axio Observer Z1 inverted microscope and 10× Plan Neofluar objective. The microscope was equipped with a Zeiss AxioCam MRm CCD camera and a Marzhauser SCAN-IM powered stage. Cultures within tissue culture Petri dishes (Greiner) were kept in a stage-mounted incubator (Cell Movie) providing 37 ℃ and a humidified 5% CO_2 atmosphere. Stage positioning, focusing and image collection were controlled by Zeiss Axiovision 4.8 software and a custom experiment manager software module. Phase contrast images were collected every hour from multiple microscopic fields for durations up to 4 days. This optical system was also used for taking brightfield images of fixed and toluidine blue-stained cultures for sprout analysis. Microscopic images were processed using NIH ImageJ software.

Invasion assay

Spheroids of SPC111 or P31 cells were transferred onto TC plastic or fibronectin-coated (5 µg/mL, Sigma Aldrich, St. Louis, MO, F1141-1MG) surfaces. Other spheroids were embedded in collagen type I gels (1.7 mg/mL, Corning, New York, NY, 354236) and were prepared following the manufacturer's instructions. Finally, some aggregates were embedded in combined collagen/fibronectin gels, which was produced by mixing fibronectin (10 µg/mL final concentration Sigma Aldrich, St. Louis, MO, F1141-1MG), human factor FXIII (2 U/mL) and thrombin (0.2 U/mL, Sigma Aldrich, St. Louis, MO, T6884-1KU) to 1.7 mg/mL collagen type I gel.

Gels were made and kept in 6 mm diameter PLA wells, 3D printed on 35-mm culture dishes (29). First, 30 µL gel solution was poured into the wells and was allowed to form a 0.5-mm thick gel (measured at the center of the well) at 37 ℃ for 30 min. Then to each well, a few spheroids were added within an additional 30 µL of gel solution, which was layered on the surface of the already solid hydrogel. After gelation at 37 ℃, for 30 min the 1 mm thick spheroid-containing gel sandwiches were submerged in DMEM medium supplemented 10% FBS (Sigma Aldrich, St. Louis, MO, F9665). Multi-field phase-contrast mosaic images of

the aggregates were taken after seeding and after 48 hours by using a Leica DM IRB inverted microscope equipped with a motorized stage (Marzhauser SCAN-IM), a 10X HC-PLAN objective (NA 0.25, working distance 11.0 mm), and an Olympus DP70 CCD camera.

Statistical analysis

Four radii of invaded area around of each aggregate were measured using ImageJ. Average values were determined, then each average radius was normalized by the average radius of original aggregates (R/R0). At least 7 aggregates were measured and averaged for each substrate and each cell line. Error bars represent the SEM. Statistical analyses were performed using Student's unpaired *t*-test.

Endothelial sprouting (ES) anisotropy analysis

Anisotropy of the sprout arbor growing from endothelial (HUVEC) aggregates in contact with MPM spheroids in fibrin gel co-cultures was measured on the basis of sprout morphology and by using a modified Sholl analysis (31) developed earlier (32). The source code of the algorithm is shared at https://github.com/gulyasmarton/SproutAnalysis/. Brightfield z-stack images with z-steps of 20 µm were collected from the sprouting cell aggregates fixed with 4% paraformaldehyde and stained with toluidine-blue. The ImageJ software was used to segment the images for individual sprout identification. Based on the binarized 2D images and the optical system's depth-of-field parameter (10 microns), we generated voxels and created a 3D reconstruction of the entire volume of the sprout arbor.

Next, we inserted concentric cylinders separated with a radial distance of 20 µm into the reconstructed volume and identified areas where sprout segments traversed the cylinder surfaces. We applied the ImageJ particle detection algorithm (33) to identify individual sprouts. We used these identified sprout segments to create vectors pointing from the center to a given cylinder. Vectors were then normalized into the unit range and averaged to yield the anisotropy value for each sprout arbor. Thus, the value 0 corresponds to a fully isotropic arbor morphology while 1 corresponds to a fully anisotropic arbor where all sprouts extend in the same direction. The sprout anisotropy measure was calculated for several sprout arbors and the pooled data were subjected to statistical analysis.

Animals

Eight-week-old male SCID mice were obtained from the animal facility of the 1st Department of Pathology and Experimental Cancer Research of Semmelweis University. In total, 53 SCID mice were used for the SPC111 model, whereas P31 cells were injected into 30 mice. Notably, an additional 18 mice were also used for the SPC111-VEGF-A model.

According to the institutional animal welfare guidelines, all mice were maintained on a daily 12-h light/12-h dark cycle and were housed under pathogen-free conditions in microisolator cages with laboratory chow and water ad libitum. Body weights were monitored every other day, animals demonstrating severe stress or 20% of weight loss were euthanized.

The animal study protocols were conducted according to National Institute of Health (NIH) guidelines for animal care and were approved by the Animal Care and Use Committee of Semmelweis University (permission No. PEI/001/2457-6/2015).

Orthotopic MPM model

Under anesthesia (Ketamine-Xylazine, 80:12 mg/kg, Sigma Aldrich, St. Louis, MO, K113), a midline incision was made on the chest, muscles on the right side were separated and cells (2×10^6 SCP111 cells or 1×10^6 P31 cells) were injected between the 2nd and 3rd ribs. Before the tumor cell inoculation, the analgesic, butorphanol (0.4 mg/ttkg; Alvegesic, ALVETRA Vienna, Austria) were administered intramuscularly. Animals were sacrificed after 5, 7, 12, 21, 24, 29, 31 and 35 days after SPC111 cell injection, 4, 42 and 52 days after P31 cell injection and 3, 4 and 7 days after SPC111-RFP-VEGF-A cell injection.

Immunofluorescence analysis: *frozen sections*

The diaphragm was removed, then tumors were cut out and embedded into cryomatrix (Thermo Fisher Scientific, Waltham, MA, 6769006) as follows: Cryomolds (Tissue-tek Cryomold, VWR, Radnor, PA, 102094-040) were filled half full with cryomatrix and were frozen in isopentane (Sigma-Aldrich St. Louis, MO, 277258) chilled with liquid nitrogen. Cut-out diaphragms with tumors were put onto a teflon card and were frozen to ensure that the samples remain flat. The frozen samples were put on the top of the frozen cryomatrix and the mold was filled with cryomatrix

Table 1 Antibodies and fluorescent dyes used for immunofluorescence

Antibody	Species	Manufacturer	Catalog number	RRID	Dilution
CD31	Rat monoclonal	BD Pharmingen, Franklin Lakes, NJ	550274	AB_393571	1:50
Laminin	Rabbit polyclonal	DAKO (Agilent), Santa Clara CA	Z0097	AB_2313665	1:200
PanCK	Rabbit polyclonal	Invitrogen	180059		1:100
BrdU	Mouse monoclonal	BD Biosciences, San Jose, CA	347580	AB_400326	1:50
SMA	Mouse monoclonal	DAKO (Agilent), Santa Clara CA	M0851	AB_2223500	1:200
Fibronectin	Rabbit polyclonal	Merck KGaA, Darmstadt, Germany	AB2033	AB_2105702	1:200
Human Collagen I.	Rabbit polyclonal	Merck KGaA, Darmstadt, Germany	HPA011795	AB_1847088	1:50
Collagen I.	Rabbit polyclonal	Thermo Fisher Scientific, Waltham, MA	PA1-26204	AB_2260734	1:50
Lyve-1	Rabbit polyclonal	ReliaTech GMBH, Wolfenbüttel, Germany	103-PA50-AG	AB_2876870	1:200
Alexa Fluor 488	Donkey-anti-rat	Thermo Fisher Scientific, Waltham, MA	A-21208	AB_2535794	1:400
Alexa Fluor 488	Donkey-anti-mouse	Thermo Fisher Scientific, Waltham, MA	A-21202	AB_141607	1:400
Alexa Fluor 555	Donkey-anti-mouse	Thermo Fisher Scientific, Waltham, MA	A-31570	AB_2536180	1:400
Alexa Fluor 555	Donkey-anti-rabbit	Thermo Fisher Scientific, Waltham, MA	A-31572	AB_162543	1:400
DAPI (100 µg/mL)	–	Sigma Aldrich, St. Louis, MO	32670	–	1:50
TOTO-3 (1 mM)	–	Invitrogen, Carlsbad, CA	T3604	–	1:500

and quickly frozen. Frozen sections cut perpendicular to the surface of the diaphragm (15 µm) were fixed in methanol (at –20 ℃) for 10 minutes and incubated at room temperature for 1 hour with a mixture of primary antibodies (*Table 1*). After washing, sections were incubated for 30 min with appropriate secondary antibodies (Life Technologies, Carlsbad, CA) (*Table 1*). Samples were analyzed by confocal laser scanning microscopy using the Bio-Rad MRC-1024 system (Bio-Rad, Hercules, CA).

Determination of the tumor cell proliferation index (PI)

Animals received 200 mg/kg bromodeoxyuridine (BrdU, Sigma-Aldrich, St. Louis, MO, B5002) 1 hour prior to termination. Immunolabeled (PanCK, BrdU, DAPI) and scanned (Pannoramic Scanner, 3D-Histech Ltd., Budapest, Hungary) frozen sections of SPC111 tumor colonies were divided into four quarters according to the supply of the nutrients (Q1: area of the tumor facing the lung, Q2: area of the tumor facing the diaphragm, Q3, Q4: area of the tumor facing the vascular proliferations located at the two sides of the sectioned tumor colonies. Proliferating (BrdU labeled) and all tumor cells (DAPI) were counted (Pannoramic Viewer software, 3D-Histech Ltd., Budapest, Hungary). The proliferation index (PI) was defined according to the next formula: PI (%) = (number of proliferating cells/number of all cells) ×100. Presence of vascular proliferations and lack of intratumoral vessels was monitored by appropriate serial sections (CD31, laminin) from at least 4 different depths of the tumor nodules. Samples containing intratumoral vessels were omitted. The average size of the examined tumors was 1,034±255 × 355±77 µm. Statistical significance of difference between the PIs of the four quarters was analyzed by using Student's *t*-test. Results were considered as significant at $P \leq 0.05$.

Immunofluorescence analysis: whole-mount samples

Animals were sacrificed by anesthetic overdose (Ketamine-Xylazine, Sigma Aldrich, St. Louis, MO, K113). The diaphragm was fixed by injecting 2% paraformaldehyde (4 ℃) into the abdomen (2 mL) and into the thorax (1 mL). After 15 min, the diaphragm was removed and washed in phosphate buffered saline (PBS, Sigma Aldrich, St. Louis, MO, P5493). The sample was permeabilized with 1.25% Triton-X 100 (Sigma Aldrich, St. Louis, MO, T9284) (15 min, RT). After washing, samples were incubated overnight with CD31 antibody (*Table 1*). After 8 hours

of washing in PBS, samples were incubated overnight with the appropriate secondary antibody (*Table 1*). After another 8-hour washing, samples were put onto slides, covered (Fluorescence mounting medium, DAKO Agilent Pathology Solutions, Santa Clara, CA, S3023) and analyzed by confocal laser scanning microscopy using the Bio-Rad MRC-1024 system (Bio-Rad, Hercules, CA).

Electron microscopy

Tumor-bearing animals were anesthetized as mentioned above and perfused via the left ventricle with PBS for 10 min and with a mixture of 4% paraformaldehyde and 1% glutaraldehyde in PBS for 15 min at room temperature. Diaphragms with tumors were removed, cut into 1–2 mm pieces and immersed in the same fixative for an additional 2 hours. Pieces were post-fixed in 1% OsO_4 and 0.5% K-ferrocyanide in PBS for 2 hours, dehydrated in a graded series of acetone and embedded in Spurr's mixture (Sigma Aldrich, St. Louis, MO. EM0300). Samples were analyzed on semithin sections stained by 0.5% toluidine blue (pH 8.5). Ultrathin sections, cut by an RMC MT-7 ultramicrotome (Research and Manufacturing Co., Tucson, AZ), were contrasted with uranyl-acetate and lead citrate and analyzed using a Philips CM10 electron microscope (Eindhoven, Netherlands).

RNA isolation, reverse transcription and real-time qPCR

Isolation of total RNA from cell lines was performed using TRIzol Reagent (Life Technologies, Carlsbad, CA, 15596026). Contaminating DNA was removed with TURBO DNA-free kit (Ambion, Austin, TX, AM1907). One µg total RNA per sample was reverse-transcribed with a high-capacity cDNA reverse transcription kit as recommended by the supplier (Life Technologies, Carlsbad, CA, 4368814).

Real-time qPCR was performed by the ABI 7500 Fast Real-time PCR system (Applied Biosystems, Foster City, CA), using ABI TaqMan assay for COL1A1 (Assay ID: Hs00164004_m1), according to the manufacturer's (Life Technologies, Carlsbad, CA) instructions. GAPDH (Assay ID: Hs02786624_g1) was used as endogenous control. The relative gene expression was calculated using the ΔΔC(T) method described by Livak and Schmittgen (34).

ELISA

MPM cells were seeded in appropriate culture medium. On the next day, medium was replaced with serum-free medium and cells were incubated for 24 hours. Supernatant was collected, centrifuged at 800 rpm for 5 min, frozen and stored at –80 ℃. Adherent cells were lysed in RIPA buffer (Fisher Scientific, Hampton, NH, 89900) and protein concentration was determined using the Pierce BCA kit (Thermo Fisher Scientific, Waltham, MA, 23225). VEGF-A was measured in the supernatant by ELISA (R&D-Systems, Minneapolis, MN, DVE00; RRID:AB 2800364) and secretion was calculated as pg VEGF-A/mL.

Results

MPM nodules stimulate pleural angiogenesis both peritumorally and distant from the tumor site

To study the mechanisms of tumor vascularization in MPM under experimental conditions *in vivo*, human MPM cell lines were injected orthotopically into the pleural cavity of SCID mice. Colonies formed by both cell lines were allowed to grow until the animals became moribund. Notably, the number of days elapsed until the mice became moribund was lower in case of the SPC111 cell line (*vs.* P31 cells, 28–35 *vs.* 42–52 days, respectively). MPM nodules at these time points were observable all over the chest cavity including the diaphragmatic (*Figure 1A*) and costal (*Figure 1B*) surfaces of the parietal pleura. In case of both MPM cell lines, the size of the nodules ranged between 1 and 3 mm in diameter. Of note, however, SPC111 cells reached this nodule size slightly faster, thus explaining why the mice inoculated with this cell line became moribund earlier than the ones inoculated with P31. Next, the diaphragm was removed and analyzed by confocal (whole mount preparation and frozen sections) and electron microscopy. Importantly, neither the pattern of mesothelial implantation nor the morphological aspects of proliferation differed between the two cells. Specifically, as shown in *Figure 1C,1D*, both MPM cell lines induced dense, tortuous vascular proliferations bulging into the pleural space and covering large areas of the diaphragm. Regardless of the duration of the experiment, these vascular plexuses were not necessarily confined to regions covered by MPM nodules, but were found throughout the surface of the diaphragm including areas free of tumor colonies (*Figure 1C,1D*). Tumor-independent vascular plexus growth along the pleural surface was observed in both groups and these deposits were homogenous between cell lines.

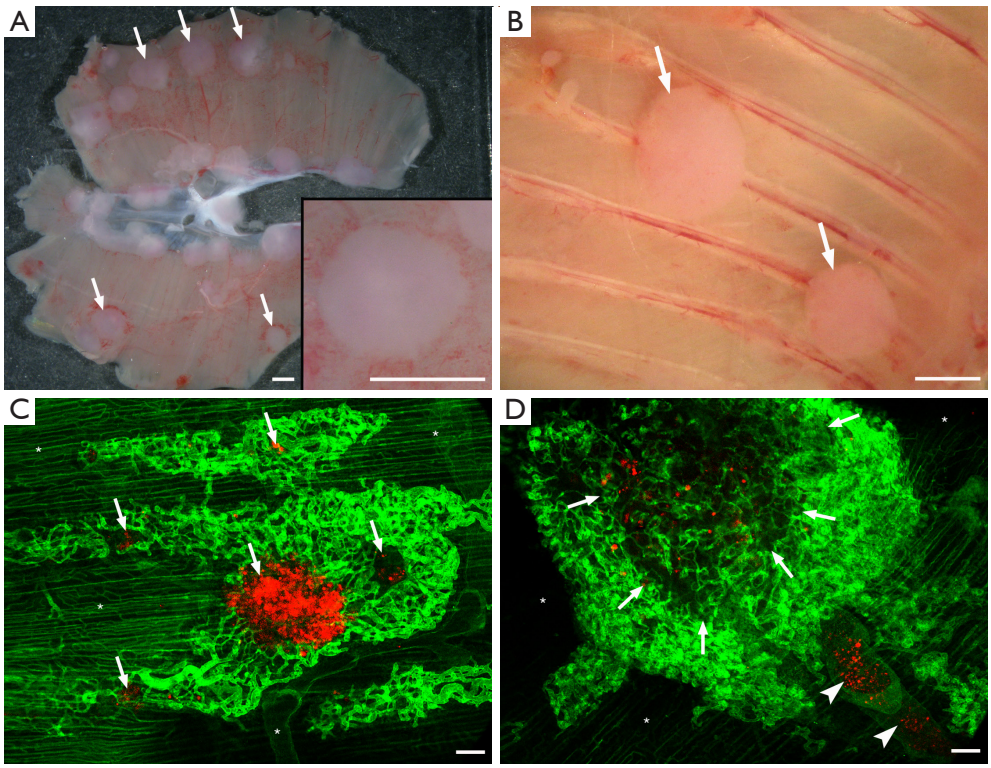

Figure 1 Malignant pleural mesothelioma (MPM) nodules on the surfaces of the chest cavity. (A) SPC111 nodules scattered on the entire surface of the diaphragm 24 days after injection of tumor cells. Arrows point at representative nodules. Inset shows a single nodule surrounded by highly vascularized area which is composed of dilated vessels with congestion. Scale bar (A and inset): 1 mm. (B) P31 nodules 42 days after orthotopic injection of tumor cells (arrows) located on the costal surface of the parietal pleura. Scale bar: 1 mm. (C) SPC111 colonies (mCherry, red, arrows) on the surface of the diaphragm 21 days after tumor cell injection. Whole mount immunostaining for CD31 (green). Small colonies (arrows) are surrounded by vascular proliferations. The vessels of the vascular proliferations are dilated and arranged irregularly compared to the normal vessels in the diaphragm which are narrow and run in a parallel manner. Representative parts of the tumor-free areas are marked with asterisks. Scale bar: 100 µm. (D) Whole mount immunostaining of the diaphragm for CD31 (green) 52 days after P31 tumor cell (mCherry, red) injection. The mCherry expression of P31 cells in this colony is low. For better orientation, arrows point at the periphery of the nodule. Vascular proliferations are present around the nodule but vessels are visible also inside the nodule. The vessels of the vascular proliferations are dilated and arranged irregularly compared to the normal vessels in the diaphragm which are narrow and run in a parallel manner. Tumor cells are visible in the efferent lymphatic vessel (arrowheads). Representative parts of the tumor-free areas are marked with asterisks. Scale bar: 100 µm.

MPM-induced vascular plexus formation utilizes both ES and IA

In order to gain a deeper understanding of MPM-induced angiogenesis, we thoroughly examined the development of the aforementioned vascular plexuses. Notably, the growing capillary plexuses elevated above the original diaphragmatic surface but remained covered by the mesothelium (Figure S1A,S1B). 3D reconstruction of CD31 stained samples revealed numerous blind endothelial sprouts and pillars of different sizes within these capillary plexuses (*Figure 2A,2B*). Transluminal pillar formation within vessel lumens is the first step and a characteristic feature of IA (35). The structure of these pillars was analyzed by electron microscopy. Close to the level of the original surface of the diaphragm the pillars contained collagen bundles, which are basal components of these structures (35) (*Figure 2C*). Farther above the original surface of the diaphragm the pillars contained amorphous ECM, rich in fibronectin, instead of the collagen bundles (*Figure 2D*). Accordingly, at this level, capillaries were embedded in a loose fibronectin-

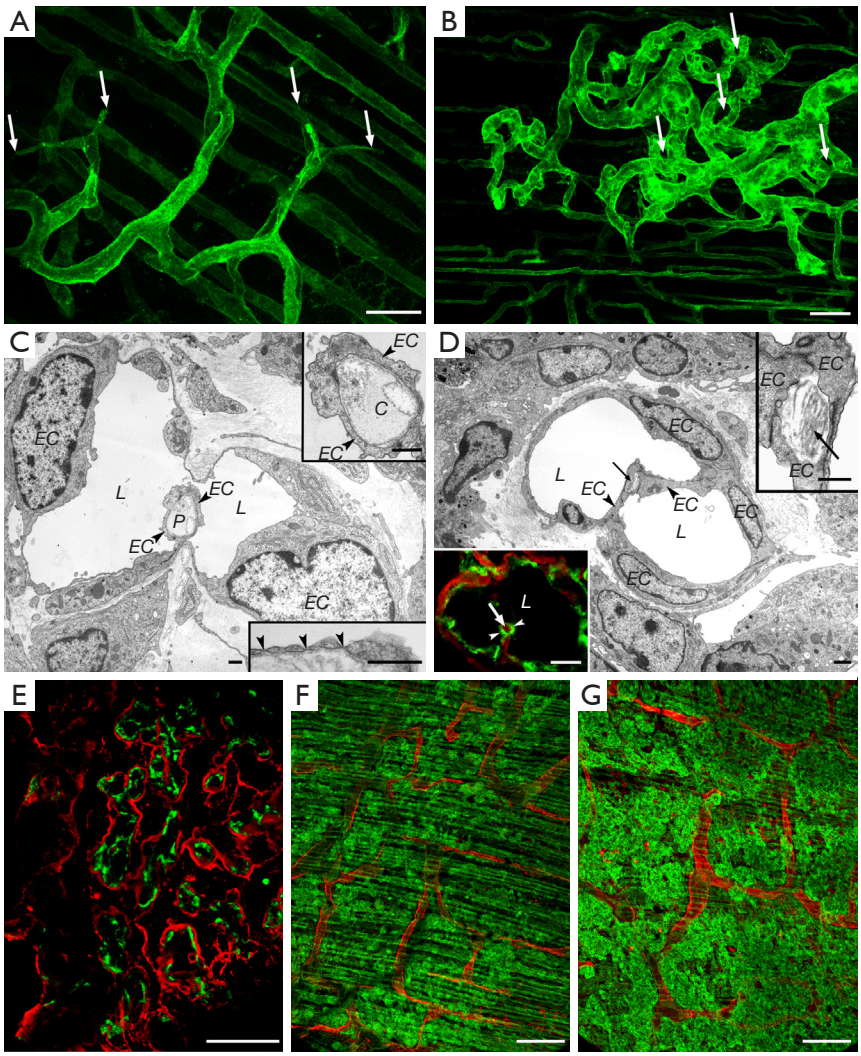

Figure 2 Malignant pleural mesothelioma (MPM)-induced vascular plexus formation. (A) Early stage of formation of vascular proliferations. Horizontal view of 104 optical sections (step size 0.3 µm) of a whole mount sample 12 days after SPC111 tumor cell injection. CD31 (green) staining shows numerous endothelial sprouts (arrows) which are located above the original vasculature of the diaphragm. Scale bar: 25 µm. (B) Early stage of formation of vascular proliferations. CD31 (green) staining 5 days after SPC111 tumor cell injection. Horizontal view of 77 optical sections (step size 0.5 µm). Pillars of different size (hallmarks of intussusceptive angiogenesis) appear as black holes (arrows) within the tortuous vascular plexus. Scale bar: 50 µm. (C) Electron micrograph of a vessel close to the level of the original surface of the diaphragm. Cross section of a pillar (P) is visible within the vessel lumen (L). Right upper inset: the pillar is composed of a collagen core (C) which is covered by endothelial cells (EC). Right lower inset: the endothelium of the vessels undergoing intussusceptive angiogenesis contains fenestrations (arrows). Scale bar: 1 µm (C, and C insets). (D) Electron micrograph of a vessel containing a pillar (arrow) within a vascular plexus. The vessel is above the original surface of the diaphragm. Right upper inset: higher magnification shows amorphous material in the core of the pillar (arrow) which is covered by endothelial cells (ECs). Left lower inset: immunohistochemical staining shows that in a capillary lumen (L) fibronectin (red) is located in the core of a pillar (arrow) which is surrounded by CD31 (green) positive endothelial cells (arrowheads). Scale bar: 2 µm (D), 1 µm (right upper inset), 10 µm (left lower inset). (E) Capillaries (CD31, green) of the vascular proliferations located above the original surface of the diaphragm are surrounded by matrix that contains fibronectin (red). Scale bar: 25 µm. (F) Horizontal view of 39 optical sections (step size 2 µm) of a whole mount sample 4 days after injection of vascular endothelial growth factor A (VEGF-A) overexpressing SPC111 tumor cells. CD31 (green) labeling shows the appearance of the capillary plexuses throughout the whole surface of the diaphragm. Lymph vessels (Lyve-1, red) show normal morphology. Scale bar: 200 µm. (G) Horizontal view of 29 optical sections (step size 1.5 µm) of a whole mount sample 7 days after injection of VEGF-A overexpressing SPC111 tumor cells. CD31 (green) labeling shows high density of the capillary plexuses above the surface of the diaphragm. Lymph vessels (Lyve-1, red) show normal morphology. Scale bar: 200 µm.

containing matrix, concentrating around the microvessels (*Figure 2E*). This provisional matrix showed signs of maturation, characterized by the appearance of collagen fibers around the vessels (Figure S1C). The endothelium of the proliferating capillaries contained fenestrations (*Figure 2C* right lower inset) and the capillaries of the vascular plexuses were surrounded by alpha-smooth muscle actin (SMA)-positive pericytes. In contrast, pericytes of the capillaries situated deeper in the muscular layer of the diaphragm were negative for SMA (Figure S1D). In late-stage tumor nodules, SMA positive myofibroblasts were embedded in fibronectin and collagen I matrix (Figure S1E-S1G).

VEGF-A is an important promoter of vascular plexus formation

We also aimed to investigate how VEGF-A over-expression in MPM cells influences vascularization. Our studies to address this aim involved experiments with SPC111 cells stably transduced with human VEGF-A using retroviral constructs. Compared with the control SPC111-RFP cells, SPC111-RFP-VEGF-A cells secreted a much higher amount (1.97 *vs.* 10,750.47 pg/mL, respectively) of VEGF-A (Figure S2). Increased VEGF-A production by MPM cells resulted in accelerated capillary plexus formation. The development of vascular plexuses was observable from day 4 after tumor cell injection and increased dramatically by day 7 (*Figure 2F,2G*). The process culminated in the coverage of the entire surface of the diaphragm by the vascular proliferations leading to the death of the animals (day 7) even without the appearance of macroscopic tumor colonies.

Vascularization of orthotopically growing human MPM xenografts occurs through two distinct mechanisms

We analyzed the development and role of the aforementioned vascular structures in the growth of SPC111 and P31 MPM cell lines in detail. In order to be able to analyze the relationship of the developing vasculature and the tumor colonies from the earliest stage, the tumor cells were labeled by mCherry.

The vascularization of the MPM cell lines differed significantly. At the earliest time points (4–5 days following inoculation), a low number of tumor cells was located within small vascular proliferations (*Figure 3A,3B*). However, as they became larger, the SPC111 colonies pushed the vascular proliferations away and remained avascular for 2–4 weeks (*Figure 3C,3D*). In contrast, the P31 cells invaded and incorporated the network of the proliferating vessels and developed into well-vascularized tumors (*Figure 3E*).

To reveal the role of the vascular proliferations in the nutrition of the avascular SPC111 nodules, we determined the BrdU incorporation in the different regions of the tumor colonies (*Figure 3F*). According to the proliferation indexes, nutrients for the avascular tumor were provided at highest level by diffusion through the vasculature of the diaphragm. The BrdU counts of this area were followed by tumor areas next to the vascular plexuses located at the periphery of the tumor colonies. Interestingly, the lowest proliferation rate was detected at the area where the tumor faced the lungs (*Figure 3F*).

The first step of SPC111 tumor vascularization is a desmoplastic reaction at the base of the tumor nodule

Microvessels appeared in SPC111 tumors at a later stage of development, 5 weeks following inoculation (*Figure 4A*). Importantly, SPC111 vascularization was preceded by the development of desmoplastic connective tissue at the base of the tumor colonies, located predominantly at the center (*Figure 4B*). This desmoplastic matrix was subsequently invaded by the tumor evidenced by malignant cells appearing between the layers of the ECM (*Figure 4C,4D*). The process above resulted in the elevation and incorporation of an ECM network forming connective tissue paths in the avascular tumors (*Figure 4D,4E*). The matrix consisted of collagen I, fibronectin and myofibroblasts (*Figure 4A,4B*, Figure S1E-S1G). Using species-specific antibodies, we were able to demonstrate the mouse origin of this matrix (*Figure 4F*, Figure S3A). First, small capillaries originating from the vessels of the diaphragm appeared in the desmoplastic connective tissue beneath the colonies (*Figure 5A*). Later, these sprouted further inside the tumor within the connective tissue paths (*Figure 5B,5C*) and remained confined to this compartment (*Figure 4F*).

As for the ECM composition of P31 tumors, we observed large amounts of collagen I and fibronectin scattered among the tumor cells (*Figure 5D*, Figure S3B,S3C). However, in P31 tumors, the majority of collagen I was of human origin, accumulating preferentially in the tumor center (*Figure 5D*).

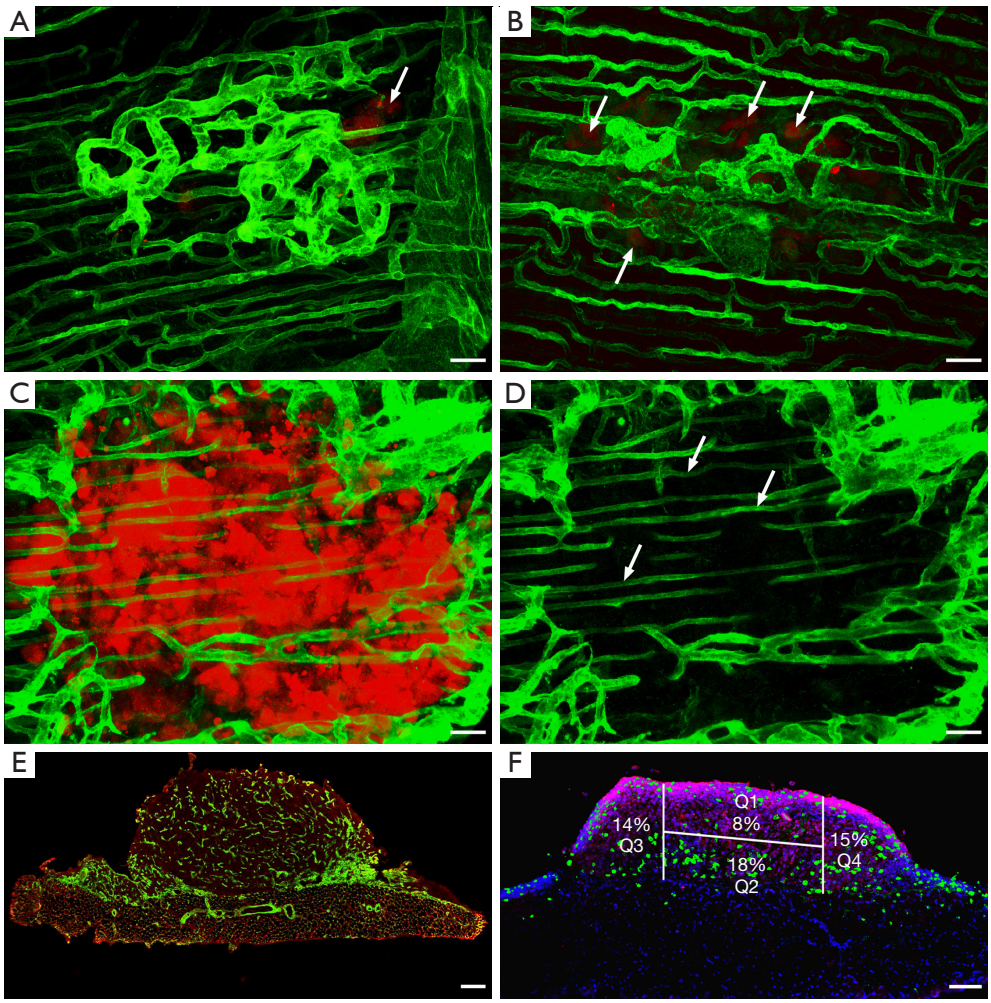

Figure 3 Vascularization of malignant pleural mesothelioma (MPM) nodules. (A) Small vascular proliferation above the original vasculature of the diaphragm. Low number of tumor cells (mCherry, red, arrow) can be observed 5 days after inoculation of SPC111 tumor cells. Horizontal view of 71 optical sections (step size 0.5 µm) of a whole mount sample stained for CD31 (green). Scale bar: 25 µm. (B) Low number of P31 tumor cells (mCherry, red, arrows) can be observed within and around the small vascular proliferation 4 days after tumor cell inoculation. Horizontal view of 53 optical sections (step size 0.5 µm) of a whole mount sample stained for CD31 (green). Scale bar: 25 µm. (C,D) SPC111 nodule (mCherry, red) 21 days after tumor inoculation on the surface of the diaphragm. Horizontal view of 70 optical sections (step size 0.6 µm). (C) The vascular proliferations (CD31, green) were pushed away by the SPC111 colony. Scale bar: 25 µm. (D) For clarity, the green (CD31) channel shows that there are no vessels within the SPC111 nodule shown in (C). Under the nodule, normally, parallel arranged vessels of the diaphragm are visible (arrows). Scale bar: 25 µm. (E) P31 nodule on day 42 is well-vascularized according to CD31 (green) labeling. Laminin (red) reveals the borders of the diaphragm and the tumor nodule. Scale bar: 200 µm. (F) Frozen section of an SPC111 nodule on day 29. To determine the proliferation rates of the different regions of the tumors, the nodules were divided in four quarters (Q1–Q4). Samples were stained for BrdU (proliferating cells, green), panCK (tumor cells, red) and TOTO-3 (all cell nuclei, blue). Scale bar: 100 µm.

Collagen-1 mRNA expression is significantly higher in the P31 cell line

ECM deposition is an important process during tumor vascularization. By using immunofluorescent staining, we found significantly higher collagen I accumulation in P31 nodules (*Figure 5D*). To validate the difference at the mRNA level, we examined the expression of the human COL1A1 gene with real-time PCR in both cell lines. We found that the relative expression level of the COL1A1

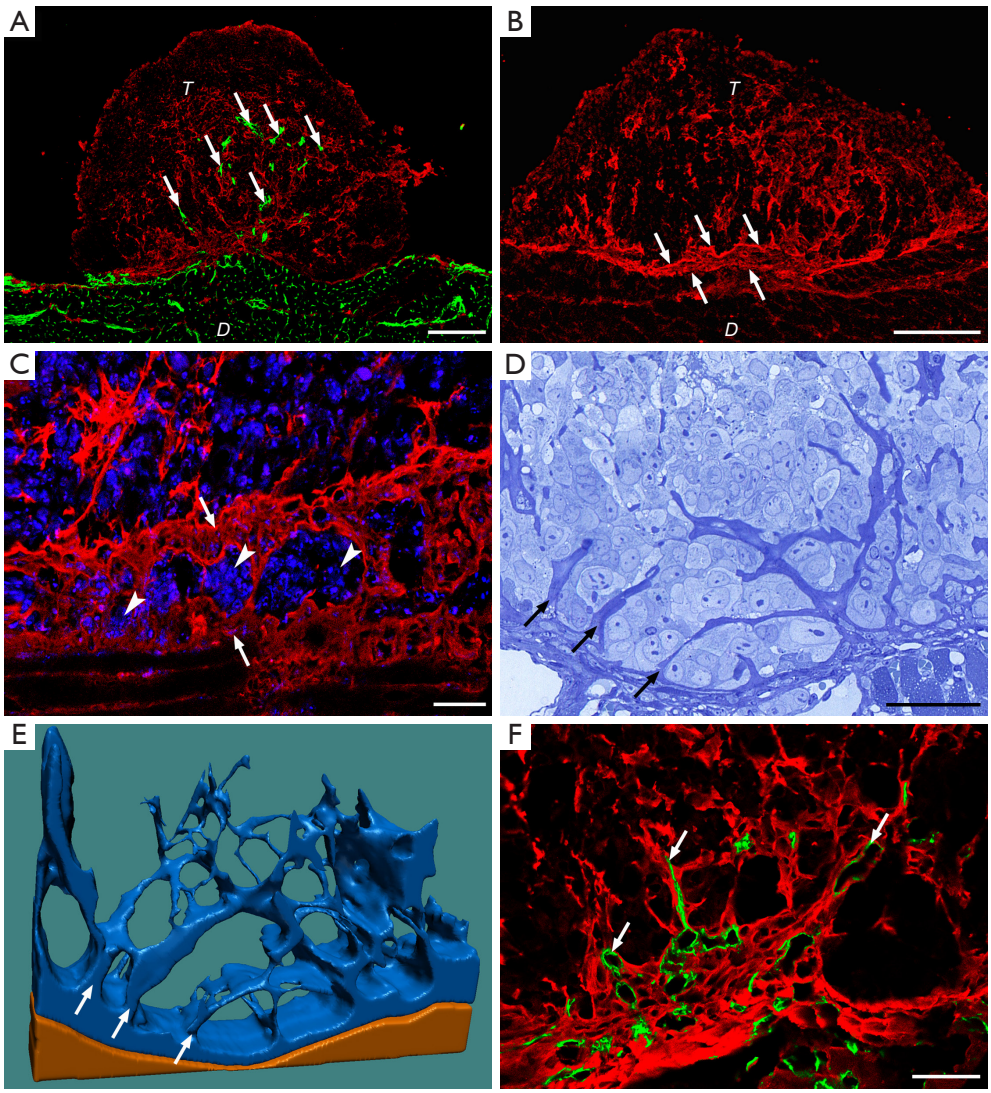

Figure 4 Vascularization of late-stage SPC111 nodules. (A) SPC111 nodule 35 days after tumor cell injection labeled for collagen type I (red) and CD31 (green). Centrally located vessels (arrows) embedded in collagen type I containing matrix are visible inside of a late-stage nodule. Tumor nodule (T), diaphragm (D). Scale bar: 200 µm. (B) Desmoplastic connective tissue (collagen type I, red) accumulated at the base (arrows) of the 29 days old SPC 111 tumor nodule (T). Scattered type I collagen is also visible within the tumor. Diaphragm (D). Scale bar: 200 µm. (C) Frozen section of a 29-day-old SPC111 tumor nodule was stained for mouse-specific collagen type I (red) and TOTO-3 (blue). The collagen containing desmoplastic matrix is separated into layers (arrows) as the tumor cells invaded (arrowheads) the matrix. Scale bar: 50 µm. (D) Toluidine blue stained semi-thin section of an SPC111 tumor shows the separated and elevated layers of the desmoplastic matrix (arrows) at the basal part of the tumor colony as a result of the invasion and growth of the tumor cells. This section is part of the three-dimensional reconstruction showed in *Figure 4E*. Scale bar: 50 µm. (E) Three-dimensional reconstruction of the connective tissue layers (blue) at the basal part of an SPC111 tumor nodule. Orange colored area represents the diaphragm. The connective tissue layers form a continuous network throughout the reconstructed tumor tissue. Note the regular layers of the matrix (arrows) elevated by the invading tumor cells. 21 serial semi-thin sections were used for the reconstruction. Tumor cells are not visible. (F) SPC111 sample on day 29 stained for CD31 (green) and mouse-specific collagen type I (red). The vessels are located at the center of the tumor base and are embedded into collagen type I containing desmoplastic matrix of mouse origin. The vessels follow the connective tissue paths towards the inner part of the nodule (arrow). Scale bar: 50 µm.

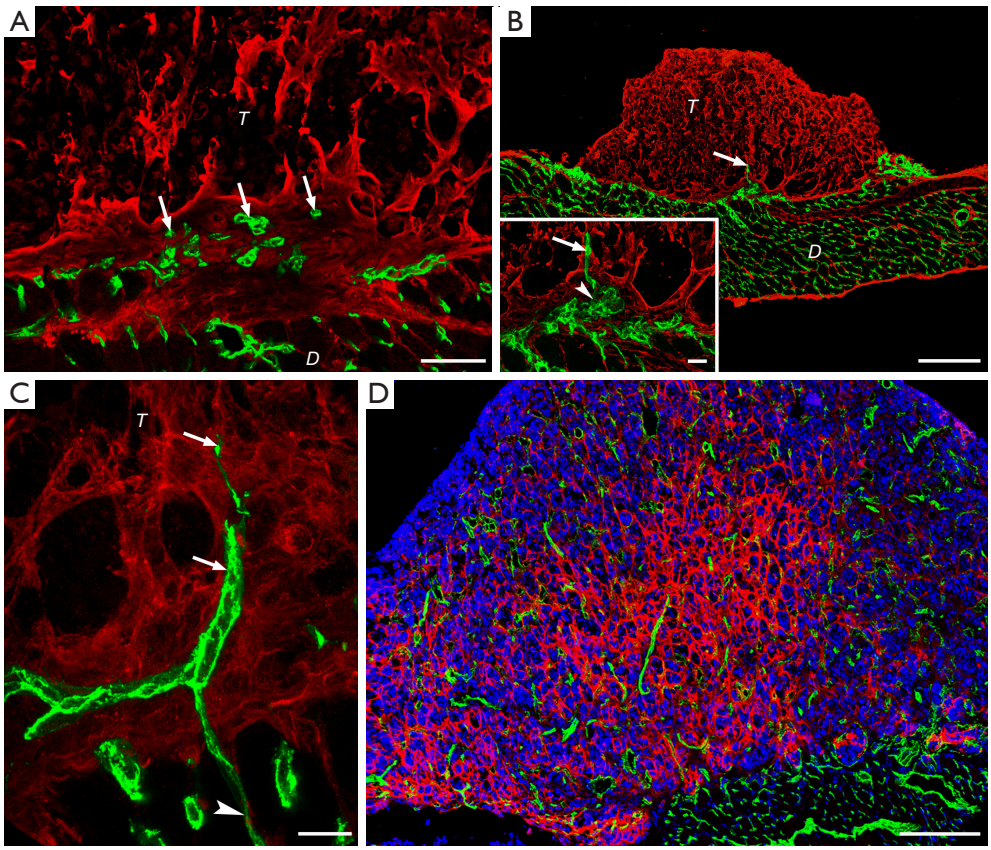

Figure 5 Sprouting in malignant pleural mesothelioma (MPM) nodules. (A) The base of an SPC111 tumor nodule 29 days after tumor cell injection. Vessels are labeled by CD31 (green), the matrix is stained by collagen type I (red). Initial phase of vascularization of the tumor nodule shows the appearance of the vessels (arrows) in the collagen containing desmoplastic matrix located beneath the tumor nodule. Diaphragm (D), tumor (T). Scale bar: 50 µm. (B) Frozen section of a 29-day-old SPC111 tumor nodule is stained for CD31 (green) and fibronectin (red). Fibronectin highlights the SPC111 tumor nodule (T) and the diaphragm (D). One vessel sprouts towards the tumor center from the desmoplastic matrix at the base of the tumor nodule (arrow) Inset: the sprouting vessel (CD31, green, arrow) is continuous with the vessels located in the desmoplastic tissue (arrowhead) (15 optical sections, step size 0.6 µm). Scale bar: 200 µm (B), 25 µm (inset). (C) The high power micrograph shows a sprout (CD31, green, arrows) oriented towards the tumor center (T) (37 optical sections, step size 0.3 µm). The sprout is embedded in collagen type I containing connective tissue (red). Note that the sprout is continuous with the vascular network of the diaphragm (arrowhead). Scale bar: 25 µm. (D) P31 tumor nodule (42 days) stained for CD31 (green), human-specific collagen type I (red) and TOTO-3 (blue). The nodule contains large amount of collagen type I (red) of human origin scattered throughout the tumor. The collagen staining shows higher intensity in the central part of the tumor. Note that the diaphragm is negative for the human-specific collagen. Scale bar: 200 µm.

was significantly higher in the P31 compared to SPC111 (Figure S4).

In addition, we have also examined the relative expression of several other transcripts of interest concerning ECM, angiogenesis, ECM production, tumor cell invasiveness, cell-cell and cell-matrix adhesion, tumor suppression, and semaphorin signaling. Notably, the relative expression of the other examined ECM components (i.e., FN1 and LOX) was also higher in the P31 than in the SPC111 tumors (nevertheless, the differences were not statistically significant) (data not shown). No such trendlines were observed in case of the other genes examined.

Interaction of MPM cells with ES in vitro

To study the influence of MPM cells on the formation of

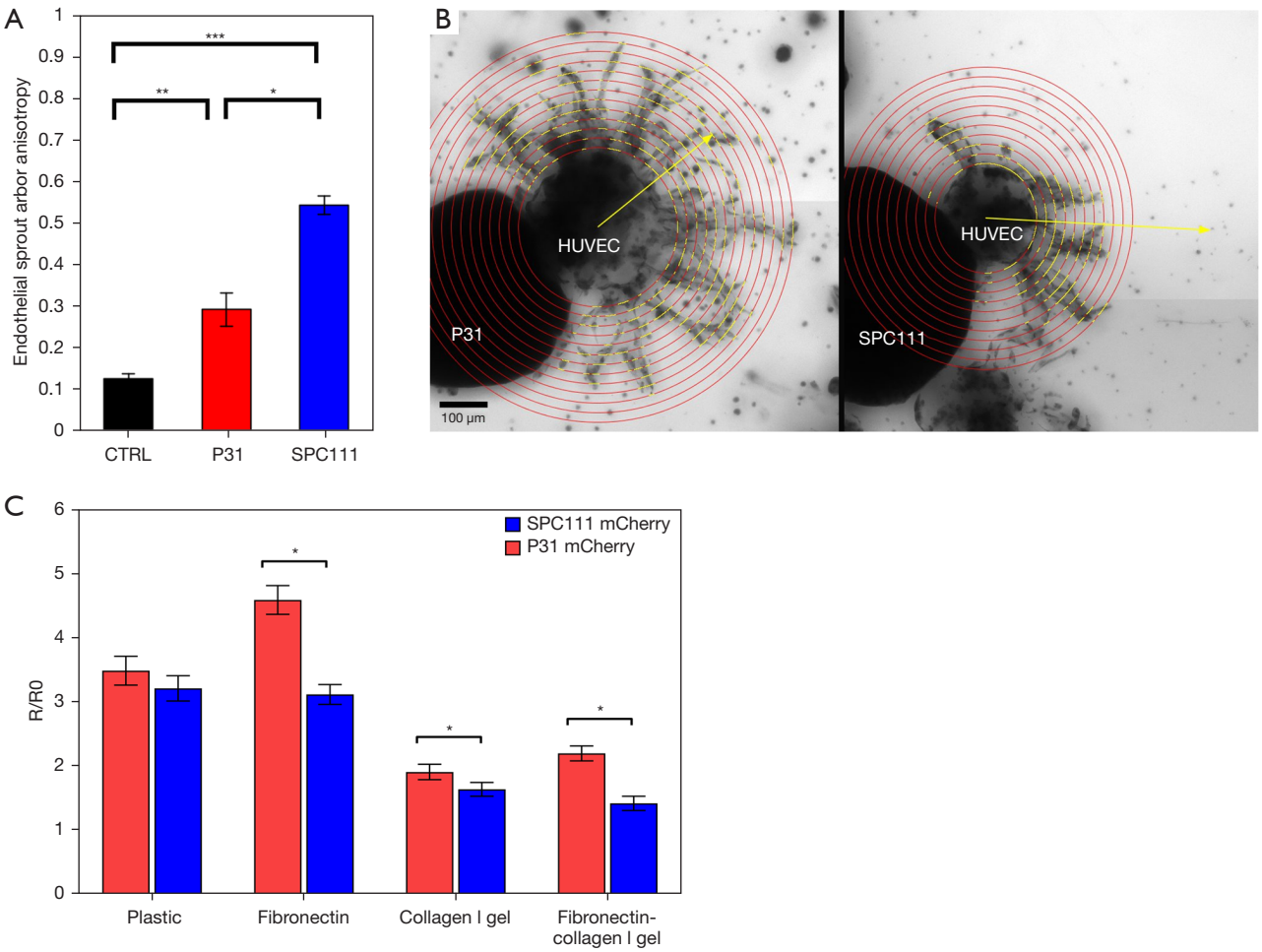

Figure 6 Malignant pleural mesothelioma (MPM) cells' *in vitro* spreading, invasive activity and interaction with endothelial cells. (A) *In vitro* endothelial sprouting morphology is influenced by the presence of MPM spheroids. Quantitative sprout arbor anisotropy analysis. Columns are mean anisotropy values (± SEM) of endothelial sprout arbors in the presence of P31 (n=5) or SPC111 (n=3) MPM spheroids. * indicate significant difference by Student's *t*-test (P*=1.07×10^{-5}, P**=7.8×10^{-4}, P***=3.1×10^{-13}). (B) Representative HUVEC aggregates with different sprout arbors developed when co-cultured for 4 days in fibrin gel with P31 (left) or SPC111 (right) MPM spheroids. Sprout anisotropy vectors (yellow arrows) indicate the distortion of developing sprout arbors by the proximity of MPM cells. Yellow segments of red circles indicate extending sprouts. Scale bar: 100 µm. (C) Spreading ability of SPC111 and P31 cell spheroids on plastic or on fibronectin coated surfaces (first four columns). Invasive activity of the spheroids in collagen type I and fibronectin/collagen type I mixed gels (second four columns). Average values were determined, then each average radius (R) was normalized by the average radius of original aggregates (R0). Significant differences are marked by * (P<0.05).

endothelial sprouts *in vitro*, we developed a co-culture assay consisting of sprout-forming aggregates of HUVEC cells and MPM spheroids of P31 or SPC111 cells. The spatial structure of multicellular HUVEC sprout arbors differed significantly in these co-cultures between the two MPM cell lines. To quantify our observations, we calculated anisotropy index values [0–1] where anisotropy of a symmetric sprout arbor is close to 0, whereas a heavily distorted arbor is characterized by an anisotropy index close to 1. SPC111 spheroids resulted in significantly higher endothelial sprout arbor anisotropy than P31 spheroids (P<0.05, *Figure 6A*). P31 spheroids permitted HUVEC sprout growth with minimal spatial distortion, whereas SPC111 spheroids repealed endothelial sprouts resulting in anisotropic sprout

arborization (*Figure 6B* and Videos S1,S2).

2D and 3D motility of MPM cells in vitro

To reveal if the difference in the vascularization of SPC111 and P31 tumors could be linked to differences in the migratory and invasive capacity of MPM cells, we also analyzed the motile and invasive activity of spheroid-forming MPM cells. In support of our *in vivo* findings, P31 cells showed significantly higher spreading (motility) on plastic and on fibronectin-coated plastic and, moreover, higher invasive capacity in collagenI and in collagenI/fibronectin containing gels (*Figure 6C*).

Discussion

While several *in vivo* murine mesothelioma models have been developed (36-39), orthotopic MPM implantation techniques have been neglected, most likely due to technical difficulties. Here we analyzed the vascularization and growth of orthotopically implanted MPM tumors in mice by using human MPM cell lines.

In both *in vivo* MPM models, intact diaphragmatic lymph vessels were located under the mesothelium but above the blood vessels. During the development of MPM-induced vascular proliferations, blood vessels appeared above the level of lymphatics. However, the whole structure remained covered by the mesothelium, which apparently moved or elevated with the proliferating vessels. This type of vascular growth closely resembles the one observed by Baluk *et al.* (40) in airways carrying an inducible VEGF-A expressing transgenic system. They observed that vessels—produced exclusively by ES and not by IA—appeared above the epithelial basement membrane, bulging into the lumen of the airways. Similar to our observation, these vessels were characterized by fenestrated endothelium. This phenomenon was also reported by others (41-43) as a characteristic feature of VEGF-A-induced angiogenesis.

Both of the used MPM cell lines secreted VEGF, although SPC111 cells secreted lower levels of VEGF-A. Therefore, we used a RFP-VEGF-A-coding retroviral construct, and were able to massively increase VEGF-A expression levels in SPC111 cells. The transgenic tumor cells induced rapid development of vascular proliferations. Eventually, the entire surface of the diaphragm was covered by tortuous microvascular structures without forming macroscopic tumor colonies, clearly indicating the decisive role of VEGF-A in capillary formation. The key role of a secreted factor (i.e., VEGF-A) was further supported by the phenomenon that microvascular proliferations were present both next to and away from the microscopic tumor colonies of the control cells. Unfortunately, due to the premature death of SPC111-RFP-VEGF-A-inoculated mice, the exact role of VEGF-A levels on the resulting tumor vascularization patterns could not be assessed.

Surprisingly, vascular proliferations did not play a crucial role in the growth of the SPC111 tumors. The inability of the tumor cells to invade the tumor-induced vasculature may lie in the cohesive strength between the tumor cells (as it was also supported by our *in vitro* experiments) resulting in the simple displacement of the proliferating vessels by the growing tumor mass. In contrast, the P31 cell line continuously incorporated the proliferating vessels. The collagen of human origin deposited by this cell line within the tumor colonies could provide "space" for further intratumoral vessel sprouting. Moreover, the other examined ECM components of human origin were as well notably higher in P31 models, further explaining the earlier development of tumor vasculature in these nodules.

A prominent vasculature in SPC111 tumors develops at a later stage of growth, and the accumulation of a desmoplastic matrix under the tumor nodule plays a key role in the vascularization process. The desmoplastic matrix together with myofibroblasts becomes incorporated into the tumor mass, perhaps by its contractile behavior (44). When the nodule contains enough ECM, it enables ES of the vasculature of the diaphragm. The majority of the accumulated connective tissue in these late-stage tumors is of mouse origin proving that this ECM was deposited by the activated fibroblasts of the diaphragm instead of the human MPM cells. In support of this, our group has shown earlier the importance of host tissue fibroblasts in tumor stroma development (24).

The most intense area of the ECM invasion and incorporation was seen in the central part at the base of the SPC111 colonies, resulting in a radial arrangement of the connective tissue in the nodules. This area is the "oldest" region of the tumor which has been in contact for the longest time with the underlying tissue. In this region, by providing a route for ES from the diaphragm, the microenvironment facilitates invasiveness unlike at the outer rim of the tumor facing the vascular proliferations and the lungs. Given the widely different angiogenic growth patterns and VEGF-A levels described in the examined cell lines, our results might explain the divergent therapeutic response to bevacizumab seen in our previous

in vivo models (12). Moreover, our data might further strengthen the hypothesis that not all patients, and not all settings, are appropriate for anti-angiogenic therapy in MPM. Of note, in this previous study, bevacizumab alone was effective only against P31 tumors and could not provide therapeutic benefit in the SPC111 model where tumor cells had markedly low baseline VEGF-A levels, as measured by ELISA (12).

Until recently, little was known about the specific tumor vasculature of MPM. To the best of our knowledge, the current study is the first to report two distinct vascular growth patterns of orthotopically implanted human MPM xenografts. Our findings are of translational relevance since these distinct vascular patterns might provide an explanation for the inconsistent therapeutic efficacies of different anti-angiogenic agents seen in previous trials and, moreover, might contribute to the development of future biomarker panels. Additionally, our results might also have potential therapeutic implications since the penetration of the majority of anticancer agents is largely dependent on tumor vasculature. Accordingly, due to poor penetration into the tumoral tissue, anticancer drugs might be less effective in MPMs with avascular, pushing growth patterns than in well-vascularized tumors characterized by invasive patterns.

A possible limitation of the current study can be that the growth of human MPM might be different, as the anatomy of the human diaphragm differs from the mouse diaphragm. In humans, under the mesothelium there is a thick but vascularized collagen layer which probably prevents the formation and elevation of vascular proliferations above the surface of the diaphragm. However, similarly to late-stage SPC111 tumors, this collagenous layer might be incorporated into the tumor and might provide connective tissue paths to enable the development of the tumor vasculature. The use of MPM cell lines and immune-deficient mice might as well constitute another potential study limitation. Although these cell line-derived xenografts are widely used by the scientific community to study the biological features of MPM and therefore, our results can be easily reproduced (45), the immunological contexts of tumorigenesis cannot be fully reconstructed in these models. Accordingly, our results require further validation in additional experimental models such as genetically engineered mouse- or asbestos-induced murine models. Finally, although the impact of histological subtypes on vascular features has not yet been demonstrated in MPM (46,47), further studies are needed to clarify whether there is a correlation between these newly described vascular growth patterns and the histological origin of the tumor cells.

In conclusion, as in other tumor types (23), vascularization can occur by multiple mechanisms in MPM. In the invasive growth pattern, MPM cells invade and thus co-opt the peritumoral capillary plexuses of the diaphragm. In the pushing/desmoplastic growth pattern, MPM cells induce a desmoplastic response within the underlying tissue which allows endothelial ingrowth and the development of a nutritive vasculature. Besides providing insights into MPM nodule formation and vascularization, our results are hypothesis-generating for following biomarker studies and might lay the framework for future personalized therapeutic strategies in MPM patients.

Acknowledgments

Funding: BD, BH and VL were supported by the Austrian Science Fund (FWF I2872 to BH; FWF I3522 to VL; FWF I3977 and I4677 to BD). BD, ZM, IH, SP and AC acknowledge funding from the Hungarian National Research, Development and Innovation Office (KH130356 and KKP126790 to BD; 2020-1.1.6-JÖVŐ and TKP2021-EGA-33 to BD and ZM; ANN128666 to IH; SNN 114490 to SP; ANN 132225 to AC). VL is a recipient of the Bolyai Research Scholarship of the Hungarian Academy of Sciences and the UNKP-19-4 New National Excellence Program of the Ministry for Innovation and Technology. ZM was supported by the UNKP-20-3 and UNKP-21-3 New National Excellence Program of the Ministry for Innovation and Technology of Hungary, and by the Hungarian Respiratory Society (MPA #2020). ZL was supported by the ESMO Translational Research Fellowship.

Footnote

Reporting Checklist: The authors have completed the ARRIVE reporting checklist. Available at https://tlcr.amegroups.com/article/view/10.21037/tlcr-21-828/rc

Data Sharing Statement: Available at https://tlcr.amegroups.com/article/view/10.21037/tlcr-21-828/dss

Peer Review File: Available at https://tlcr.amegroups.com/article/view/10.21037/tlcr-21-828/prf

Conflicts of Interest: All authors have completed the ICMJE

uniform disclosure form (available at https://tlcr.amegroups.com/article/view/10.21037/tlcr-21-828/coif). BD, BH and VL were supported by the Austrian Science Fund (FWF I2872 to BH; FWF I3522 to VL; FWF I3977 and I4677 to BD). BD, ZM, IH, SP and AC acknowledge funding from the Hungarian National Research, Development and Innovation Office (KH130356 and KKP126790 to BD; 2020-1.1.6-JÖVŐ and TKP2021-EGA-33 to BD and ZM; ANN128666 to IH; SNN 114490 to SP; ANN 132225 to AC). VL is a recipient of the Bolyai Research Scholarship of the Hungarian Academy of Sciences and the UNKP-19-4 New National Excellence Program of the Ministry for Innovation and Technology. ZM was supported by the UNKP-20-3 and UNKP-21-3 New National Excellence Program of the Ministry for Innovation and Technology of Hungary, and by the Hungarian Respiratory Society (MPA #2020). ZL was supported by the ESMO Translational Research Fellowship. The other authors have no conflicts of interest to declare.

Ethical Statement: The authors are accountable for all aspects of the work in ensuring that questions related to the accuracy or integrity of any part of the work are appropriately investigated and resolved. The study was conducted in accordance with the Declaration of Helsinki (as revised in 2013). Animal experiments were performed under a project license (No. PEI/001/2457-6/2015) granted by committee board of Animal Care and Use Committee of Semmelweis University, in compliance with National Institute of Health (NIH) guidelines for the care and use of animals.

References

1. Carbone M, Kratzke RA, Testa JR. The pathogenesis of mesothelioma. Semin Oncol 2002;29:2-17.
2. Bridda A, Padoan I, Mencarelli R, et al. Peritoneal mesothelioma: a review. MedGenMed 2007;9:32.
3. Amin W, Linkov F, Landsittel DP, et al. Factors influencing malignant mesothelioma survival: a retrospective review of the National Mesothelioma Virtual Bank cohort. F1000Res 2018;7:1184.
4. Scherpereel A, Opitz I, Berghmans T, et al. ERS/ESTS/EACTS/ESTRO guidelines for the management of malignant pleural mesothelioma. Eur Respir J 2020;55:1900953.
5. Strizzi L, Catalano A, Vianale G, et al. Vascular endothelial growth factor is an autocrine growth factor in human malignant mesothelioma. J Pathol 2001;193:468-75.
6. Langerak AW, De Laat PA, Van Der Linden-Van Beurden CA, et al. Expression of platelet-derived growth factor (PDGF) and PDGF receptors in human malignant mesothelioma in vitro and in vivo. J Pathol 1996;178:151-60.
7. Schelch K, Hoda MA, Klikovits T, et al. Fibroblast growth factor receptor inhibition is active against mesothelioma and synergizes with radio- and chemotherapy. Am J Respir Crit Care Med 2014;190:763-72.
8. Li Q, Yano S, Ogino H, et al. The therapeutic efficacy of anti vascular endothelial growth factor antibody, bevacizumab, and pemetrexed against orthotopically implanted human pleural mesothelioma cells in severe combined immunodeficient mice. Clin Cancer Res 2007;13:5918-25.
9. Ogino H, Yano S, Kakiuchi S, et al. Novel dual targeting strategy with vandetanib induces tumor cell apoptosis and inhibits angiogenesis in malignant pleural mesothelioma cells expressing RET oncogenic rearrangement. Cancer Lett 2008;265:55-66.
10. Nutt JE, O'Toole K, Gonzalez D, et al. Growth inhibition by tyrosine kinase inhibitors in mesothelioma cell lines. Eur J Cancer 2009;45:1684-91.
11. Zalcman G, Mazieres J, Margery J, et al. Bevacizumab for newly diagnosed pleural mesothelioma in the Mesothelioma Avastin Cisplatin Pemetrexed Study (MAPS): a randomised, controlled, open-label, phase 3 trial. Lancet 2016;387:1405-14.
12. Laszlo V, Valko Z, Kovacs I, et al. Nintedanib Is Active in Malignant Pleural Mesothelioma Cell Models and Inhibits Angiogenesis and Tumor Growth In Vivo. Clin Cancer Res 2018;24:3729-40.
13. Grosso F, Steele N, Novello S, et al. Nintedanib Plus Pemetrexed/Cisplatin in Patients With Malignant Pleural Mesothelioma: Phase II Results From the Randomized, Placebo-Controlled LUME-Meso Trial. J Clin Oncol 2017;35:3591-600.

14. Scagliotti GV, Gaafar R, Nowak AK, et al. Nintedanib in combination with pemetrexed and cisplatin for chemotherapy-naive patients with advanced malignant pleural mesothelioma (LUME-Meso): a double-blind, randomised, placebo-controlled phase 3 trial. Lancet Respir Med 2019;7:569-80.
15. Baas P, Boogerd W, Dalesio O, et al. Thalidomide in patients with malignant pleural mesothelioma. Lung Cancer 2005;48:291-6.
16. Mutri V, Pinto C, Giaquinta S, et al. Phase I study of sorafenib and cisplatin/pemetrexed regimen in untreated malignant pleural mesothelioma (MPM) patients: Italian SoMe Study. J Clin Oncol 2011;29:abstr 7087.
17. Nowak AK, Millward M, Francis RJ, et al. Final results of a phase II study of sunitinib as second-line therapy in malignant pleural mesothelioma (MPM). J Clin Oncol 2010;28:abstr 7036.
18. Jahan T, Gu L, Kratzke R, et al. Vatalanib in malignant mesothelioma: a phase II trial by the Cancer and Leukemia Group B (CALGB 30107). Lung Cancer 2012;76:393-6.
19. Mathy A, Baas P, Dalesio O, et al. Limited efficacy of imatinib mesylate in malignant mesothelioma: a phase II trial. Lung Cancer 2005;50:83-6.
20. Kluger HM, Dudek AZ, McCann C, et al. A phase 2 trial of dasatinib in advanced melanoma. Cancer 2011;117:2202-8.
21. Sinn K, Mosleh B, Hoda MA. Malignant pleural mesothelioma: recent developments. Curr Opin Oncol 2021;33:80-6.
22. Nowak AK, Brosseau S, Cook A, et al. Antiangiogeneic Strategies in Mesothelioma. Front Oncol 2020;10:126.
23. Döme B, Hendrix MJ, Paku S, et al. Alternative vascularization mechanisms in cancer: Pathology and therapeutic implications. Am J Pathol 2007;170:1-15.
24. Bugyik E, Szabó V, Dezső K, et al. Role of (myo)fibroblasts in the development of vascular and connective tissue structure of the C38 colorectal cancer in mice. Cancer Commun (Lond) 2018;38:46.
25. Monsky WL, Mouta Carreira C, Tsuzuki Y, et al. Role of host microenvironment in angiogenesis and microvascular functions in human breast cancer xenografts: mammary fat pad versus cranial tumors. Clin Cancer Res 2002;8:1008-13.
26. Lu P, Weaver VM, Werb Z. The extracellular matrix: a dynamic niche in cancer progression. J Cell Biol 2012;196:395-406.
27. Dvorak HF. Vascular permeability factor/vascular endothelial growth factor: a critical cytokine in tumor angiogenesis and a potential target for diagnosis and therapy. J Clin Oncol 2002;20:4368-80.
28. Helm CL, Fleury ME, Zisch AH, et al. Synergy between interstitial flow and VEGF directs capillary morphogenesis in vitro through a gradient amplification mechanism. Proc Natl Acad Sci U S A 2005;102:15779-84.
29. Gulyas M, Csiszer M, Mehes E, et al. Software tools for cell culture-related 3D printed structures. PLoS One 2018;13:e0203203.
30. Davis GE, Camarillo CW. An alpha 2 beta 1 integrin-dependent pinocytic mechanism involving intracellular vacuole formation and coalescence regulates capillary lumen and tube formation in three-dimensional collagen matrix. Exp Cell Res 1996;224:39-51.
31. SHOLL DA. Dendritic organization in the neurons of the visual and motor cortices of the cat. J Anat 1953;87:387-406.
32. Mehes E, Barath M, Gulyas M, et al. Enhanced endothelial motility and multicellular sprouting is mediated by the scaffold protein TKS4. Sci Rep 2019;9:14363.
33. Schneider CA, Rasband WS, Eliceiri KW. NIH Image to ImageJ: 25 years of image analysis. Nat Methods 2012;9:671-5.
34. Livak KJ, Schmittgen TD. Analysis of relative gene expression data using real-time quantitative PCR and the 2(-Delta Delta C(T)) Method. Methods 2001;25:402-8.
35. Paku S, Dezso K, Bugyik E, et al. A new mechanism for pillar formation during tumor-induced intussusceptive angiogenesis: inverse sprouting. Am J Pathol 2011;179:1573-85.
36. Nabavi N, Wei J, Lin D, et al. Pre-clinical Models for Malignant Mesothelioma Research: From Chemical-Induced to Patient-Derived Cancer Xenografts. Front Genet 2018;9:232.
37. Martarelli D, Catalano A, Procopio A, et al. Characterization of human malignant mesothelioma cell lines orthotopically implanted in the pleural cavity of immunodeficient mice for their ability to grow and form metastasis. BMC Cancer 2006;6:130.
38. Colin DJ, Cottet-Dumoulin D, Faivre A, et al. Experimental Model of Human Malignant Mesothelioma in Athymic Mice. Int J Mol Sci 2018;19:1881.
39. Testa JR, Berns A. Preclinical Models of Malignant Mesothelioma. Front Oncol 2020;10:101.
40. Baluk P, Lee CG, Link H, et al. Regulated angiogenesis and vascular regression in mice overexpressing vascular endothelial growth factor in airways. Am J Pathol 2004;165:1071-85.

41. Roberts WG, Palade GE. Increased microvascular permeability and endothelial fenestration induced by vascular endothelial growth factor. J Cell Sci 1995;108:2369-79.
42. Roberts WG, Palade GE. Neovasculature induced by vascular endothelial growth factor is fenestrated. Cancer Res 1997;57:765-72.
43. Esser S, Wolburg K, Wolburg H, et al. Vascular endothelial growth factor induces endothelial fenestrations in vitro. J Cell Biol 1998;140:947-59.
44. Tarnoki-Zach J, Stockhammer P, Isai DG, et al. Multicellular contractility contributes to the emergence of mesothelioma nodules. Sci Rep 2020;10:20114.
45. Blanquart C, Jaurand MC, Jean D. The Biology of Malignant Mesothelioma and the Relevance of Preclinical Models. Front Oncol 2020;10:388.
46. Edwards JG, Cox G, Andi A, et al. Angiogenesis is an independent prognostic factor in malignant mesothelioma. Br J Cancer 2001;85:863-8.
47. Pulford E, Hocking A, Griggs K, et al. Vasculogenic mimicry in malignant mesothelioma: an experimental and immunohistochemical analysis. Pathology 2016;48:650-9.

Cite this article as: Kovacs I, Bugyik E, Dezso K, Tarnoki-Zach J, Mehes E, Gulyas M, Czirok A, Lang E, Grusch M, Schelch K, Hegedus B, Horvath I, Barany N, Megyesfalvi Z, Tisza A, Lohinai Z, Hoda MA, Hoetzenecker K, Pezzella F, Paku S, Laszlo V, Dome B. Malignant pleural mesothelioma nodules remodel their surroundings to vascularize and grow. Transl Lung Cancer Res 2022;11(6):991-1008. doi: 10.21037/tlcr-21-828

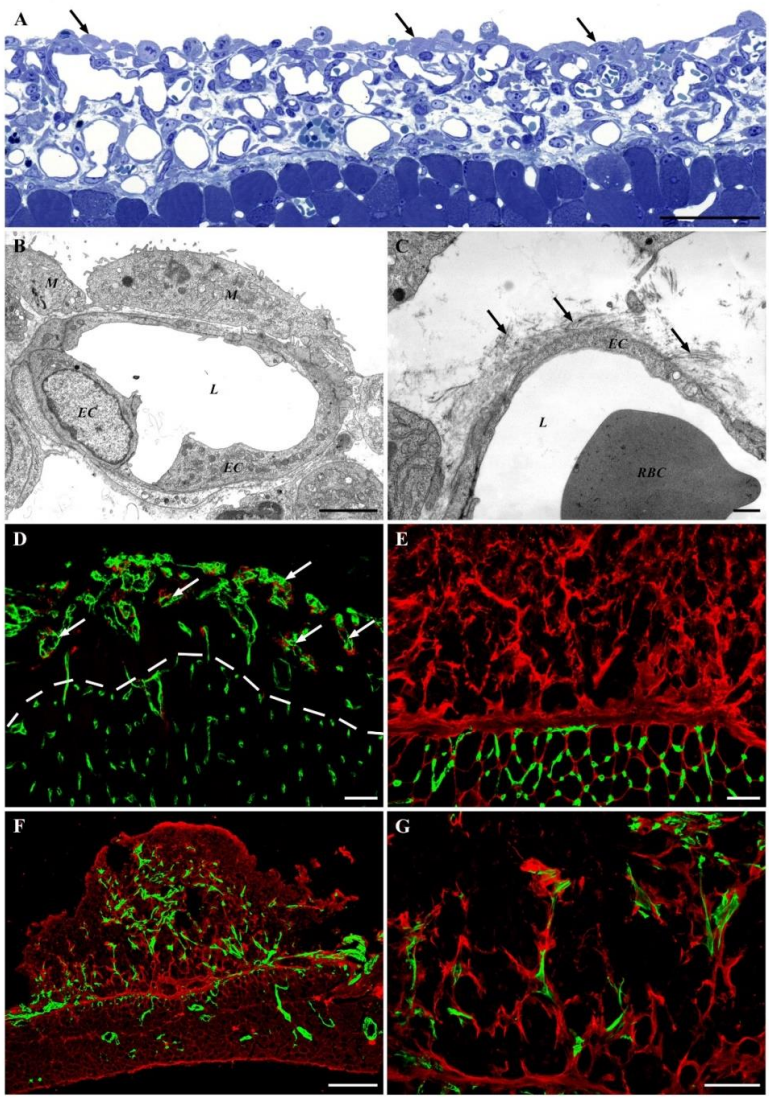

Figure S1 Processes of capillary plexus formation and extracellular matrix deposition in SPC111 tumor nodules. (A) Semi-thin cross section of a capillary plexus 35 days after SPC111 tumor cell injection. Tumor tissue is not present in this area. Vessels of the capillary plexuses elevated above the surface of the diaphragm. Arrows point at the mesothelial cover. Owing to perfusion fixation, the vessels are not collapsed and most of them do not contain erythrocytes. Scale bar: 50 µm. (B) Electron micrograph shows that the vessels are covered by mesothelial cells. Capillary lumen (L), endothelial cell (EC), mesothelial cell (M). Scale bar: 5 µm. (C) Collagen fibers (arrows) are visible around the elevated microvessel as a sign of matrix maturation. Endothelial cell (EC), capillary lumen (L), red blood cell (RBC). Scale bar: 1 µm. (D) Vascular proliferation (35 days after SPC111 tumor cell injection) elevated above the original surface (dashed line) of the diaphragm. Tumor tissue is not present in this area. The frozen section is stained for CD31 (green) and smooth muscle actin (SMA - red). Vessels of the diaphragm are negative for SMA. In contrast, the upper part shows the vessels of the capillary plexuses which are surrounded by SMA positive pericytes (arrows). Scale bar: 50 µm. (E) Avascular SPC111 tumor sample on day 21 stained for CD31 (green) and fibronectin (red). The extracellular matrix of the tumor contains fibronectin. At the lower part of the micrograph, the regularly arranged muscle fibers (appear black) are covered by fibronectin. Scattered capillaries are visible among the muscle fibers. Scale bar: 50 µm. (F) Late-stage (35 days) SPC111 sample stained for SMA (green) and collagen type I (red). The nodule contains collagen type I and SMA-positive myofibroblasts. In the diaphragm, only larger vessels are positive for SMA. Scale bar: 200 µm. (G) Late-stage (35 days) SPC111 sample stained for SMA (green) and collagen type I (red). The high power micrograph shows that the SMA-positive myofibroblasts are embedded in collagen type I containing matrix. Scale bar: 50 µm.

https://dx.doi.org/10.21037/tlcr-21-828

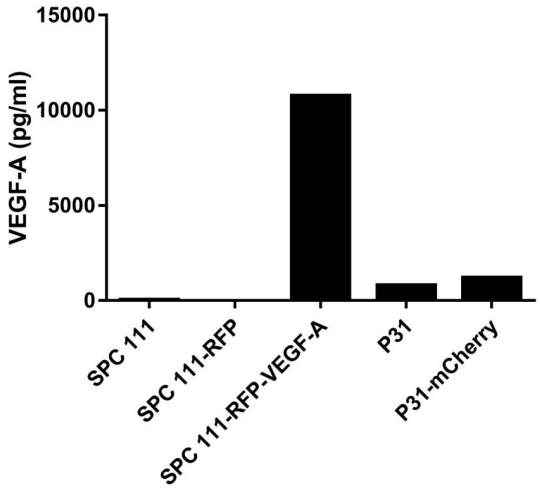

Figure S2 VEGF-A protein levels of the P31, SPC111 and transfected cell lines as measured by ELISA. Vascular endothelial growth factor A (VEGF-A) ELISA shows that compared with the control SPC111-RFP cells, SPC111-RFP-VEGF-A cells secreted 5.5×10^3-fold the amount of the key angiogenic factor, VEGF-A.

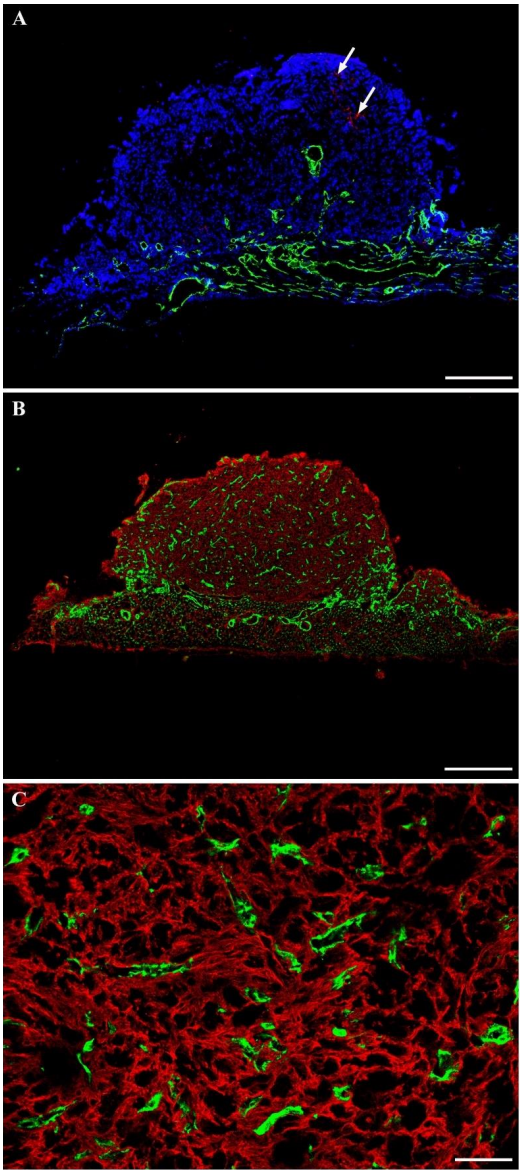

Figure S3 Extracellular matrix components of human origin are present is P31, while absent in SPC111 tumor nodules. (A) Late-stage SPC111 tumor nodule (35 days) stained for CD31 (green), human-specific collagen type I (red) and TOTO-3 (blue). The tumor is largely negative for human-specific collagen type I (red). Only a small amount of deposited human collagen type I is present (arrows). Scale bar: 200 μm. (B) P31 tumor nodule on day 42 is stained for CD31 (green) and fibronectin (red). The nodule is well-vascularized and contains large amount of fibronectin. Scale bar: 500 μm. (C) P31 tumor nodule on day 42 is stained for CD31 (green) and fibronectin (red). Higher magnification shows that large amount of fibronectin (red) is deposited evenly in the tumor and vessels are regularly arranged within the matrix. Scale bar: 50 μm.

https://dx.doi.org/10.21037/tlcr-21-828

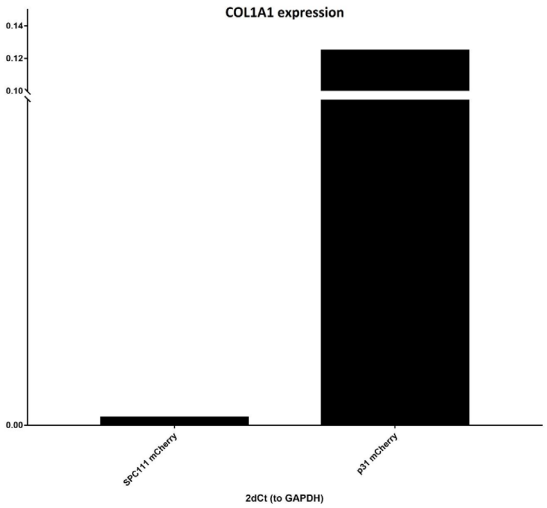

Figure S4 Comparison of COL1A1 transcript levels in P31 and SPC111 mCherry cell lines. Real-time PCR shows that the relative expression levels of COL1A1 is significantly higher in the P31 cell line.

https://dx.doi.org/10.21037/tlcr-21-828

Supplementary videos

Keywords for videos: Time-lapse microscopy, live imaging, in vitro, MPM spheroid, endothelial sprouting

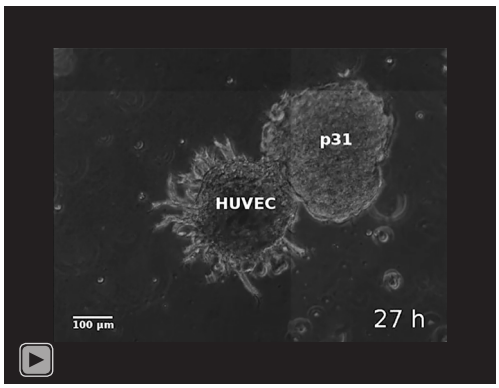

Video S1 Time-lapse video showing 4 days of sprout formation by HUVEC aggregate in fibrin extracellular matrix (ECM) gel in the presence of a P31 spheroid. Images were captured every hour by phase-contrast microscopy. Scale bar: 100 µm.

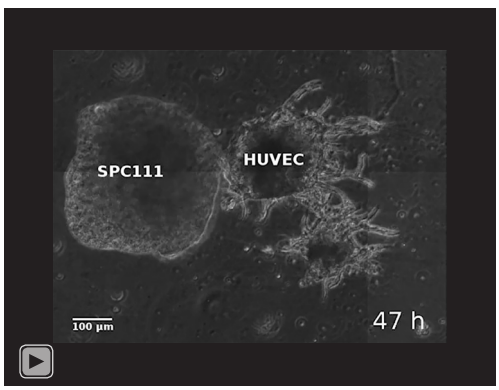

Video S2 Time-lapse video showing 4 days of sprout formation by HUVEC aggregate in fibrin ECM gel in the presence of a SPC111 spheroid. Images were captured every hour by phase-contrast microscopy. Scale bar: 100 µm.

https://dx.doi.org/10.21037/tlcr-21-828